Numerical simulations of annular disk dynamics in homogeneous and density-stratified fluids at moderate Reynolds number

A. M. Abdal,[1,2,*] D. Panda,[1] L. Kahouadji,[1] M. Shams,[1] S. Shin,[3] J. Chergui,[1] D. Juric,[4,5] and O. K. Matar[1]

[1]*Department of Chemical Engineering, Imperial College London, South Kensington Campus, London SW7 2AZ, United Kingdom*

[2]*Department of Environmental and Sustainability Engineering, College of Engineering and Energy, Abdullah Al Salem University, 12037 Kuwait City, Kuwait*

[3]*Department of Mechanical and System Design Engineering, Hongik University, Seoul 04066, Republic of Korea*

[4]*Université Paris Saclay, Centre National de la Recherche Scientifique (CNRS), Laboratoire Interdisciplinaire des Sciences du Numérique (LISN), 91400 Orsay, France*

[5]*Department of Mechanical Engineering, The University of Tokyo, 7-3-1 Hongo, Bunkyo-ku, Tokyo 113-8656, Japan*

(Received 4 February 2026; accepted 20 October 2026; published 16 November 2026)

The transport of particles in density-stratified fluids is a ubiquitous feature of natural environments. In the ocean, for example, particles and marine snow move through water columns with pronounced density variations arising from temperature and salinity gradients. Such stratification can significantly modify particle rise or settling rates and promote accumulation near sharp density transitions. Although previous work has largely focused on spherical particles, including their isolated motion, pairwise interactions, and collective transport in stratified fluids, the dynamics of nonspherical bodies with a central aperture remain less explored. Here, we examine the rising dynamics of an annular disk in both homogeneous and linearly stratified fluids using particle-resolved, three-dimensional direct numerical simulations based on an immersed-boundary method in a Cartesian domain. We quantify how the dynamics depend on the Froude and Archimedes numbers, and the diffusivity of the stratifying agent through the Schmidt number.

DOI: 10.1103/32fm-np8h

I. INTRODUCTION

The transport dynamics of particles, droplets, and bubbles in density-stratified fluids has recently drawn considerable scientific attention, reflecting their importance in numerous natural processes [1,2]. In the ocean, for example, microplastics and marine snow can rise or settle through fluid layers with varying densities caused by differences in temperature or salinity. These density gradients in the surrounding fluid can significantly alter their transport and lead to entrapment [3]. In a homogeneous fluid, the transport dynamics of a spherical particle is typically determined by the relative density ρ_p/ρ_f and particle Reynolds number, defined as $\mathrm{Re}_p = D_p U \rho_{f,0}/\mu_f$, where ρ_p is the particle density, ρ_f is the local fluid density, $\rho_{f,0}$ is the reference fluid density, D_p is the particle diameter, U

*Contact author: abdullah.abdal@aasu.edu.kw

Published by the American Physical Society under the terms of the Creative Commons Attribution 4.0 International license. Further distribution of this work must maintain attribution to the author(s) and the published article's title, journal citation, and DOI.

is its characteristic velocity, and μ_f is the fluid viscosity. In the low Re_p regime, the characteristic velocity may be taken as the Stokes velocity scale, such that $U_s = \frac{1}{18}(\rho_p - \rho_f)D_p^2 g/\mu_f$. When the role of inertia increases, a Reynolds number based on a gravitational velocity scale is typically used, because the particle velocity is an emergent property of the system.

In a density-stratified fluid, Doostmohammadi *et al.* [4] demonstrated that spherical particles that settle under the influence of gravity accelerate until they reach a maximum velocity magnitude, followed by either a monotonic deceleration or an oscillatory speed depending on the stratification strength. The stratification strength is measured through the Froude number, as defined in Sec. II. The caudal fluid, entrained by the sphere's motion, forms a jet in the region behind the settling spherical particle due to the restoration of the perturbed isopycnals back to their neutrally buoyant position. The strength of the jet depends on the molecular diffusivity of the stratifying agent. Previous works have also shown that spherical particles settling in a density-stratified ambient fluid experience an enhanced drag [5,6], caused by local variations in buoyancy force and the complex vorticity structure in the particle's wake. Furthermore, in strongly stratified fluids, particles may levitate or reverse direction momentarily prior to reaching a neutrally buoyant position. This counterintuitive behavior was demonstrated experimentally by Abaid *et al.* [7] in a sharply stratified, three-layer fluid, and has since been further explored by Camassa *et al.* [8] using potential energy arguments and by Wang *et al.* [9] via a detailed force balance analysis. Notably, this behavior has been mainly observed in salt-stratified fluids with small molecular diffusivity. In such cases, particles often settle under large Reynolds numbers before approaching the density transition layer, which makes fully resolved three-dimensional direct numerical simulations (DNSs) challenging due to the thin boundary layers associated with such flows.

Previous works for settling disks [10,11] and spheroids [12–14] have shown a tendency to reorient under strong stratification. Experiments by Mrokowska [15,16] examined the coupled evolution of settling velocity, orientation, and wake structure for solid disks crossing a nonlinear density transition between two homogeneous layers, whereas the present study considers rising solid and annular disks in a linearly stratified fluid. Reorientation was found to be related to the dominance of the buoyancy induced torque over the hydrodynamic torque [13]. At small Reynolds numbers, Varanasi *et al.* [17] theoretically examined the rotation of settling spheroids in a linearly stratified fluid, accounting for weak inertial corrections, hydrostatic effects, and hydrodynamic effects arising from perturbations of the density field, with the latter depending on scalar diffusion. At larger Reynolds numbers, Lam *et al.* [18] have shown that the buoyancy torque can also dampen the orientation dynamics of the fluttering disks. Moreover, stratification tends to prohibit the lateral motion observed for disks and spheroids found in homogeneous fluids beyond a critical Reynolds number [19,20]. A regime map for the disk dynamics in a homogeneous fluid was provided by Field *et al.* [21] based on the disk Reynolds number and its moment of inertia, I. The regime map shows that the disk path may be steady (rectilinear), fluttering, chaotic, or tumbling. The numerical work of Auguste *et al.* [22] at moderate Reynolds numbers has extended this regime map to include two additional subregimes for fluttering and tumbling disks, namely, a hula hoop regime and a helical autorotation regime. Vincent *et al.* [23] found that the introduction of a hole in the center of the disk can alter the observed settling regime. For example, a tumbling disk may transition to the chaotic regime (which is seen to be more stable) if the ratio of the hole size and the diameter of the disk, d/D_D, is sufficiently large. In their work, they found that most regime transitions occur when $d/D_D \simeq 0.3 \pm 0.1$, but remain dependent on I. Thus, adding a central perforation is generally considered to be stabilizing in a homogeneous fluid.

In this work, we perform DNSs of a rising disk with a central perforation where the particle density is similar to that of the ambient fluid. We consider both a homogeneous fluid and a density-stratified fluid, starting from the fluttering regime as seen in the experiments of Fernandes *et al.* [19]. The findings in this work are consistent with previous work in homogeneous and density-stratified ambient fluids, but go beyond the current numerical and experimental observations. The present results may be relevant to a range of oceanic applications, including the transport of microplastic debris that are nearly neutrally buoyant and often irregular in shape.

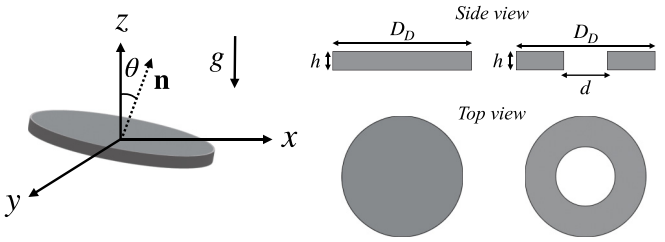


FIG. 1. Schematic of the disk geometry. The coordinate system, gravity direction, and inclination angle θ between the disk normal $\boldsymbol{n}$ and the vertical z axis are shown. Side and top views compare a solid disk and a perforated disk of outer diameter D_D and thickness h, with a central hole of diameter d.

The paper is organized as follows: Section II presents the numerical method used in this work, the numerical results and relative comparisons with the literature are presented in Sec. III, and we conclude in Sec. IV.

II. METHODS

A. Governing equations and numerical methods

In this work, we consider the rising dynamics of a disk starting from rest in both a homogeneous and a density-stratified fluid. The motion of the disk and its interaction with the surrounding stratified fluid are modeled using a fictitious domain method, so the mass and momentum conservation equations are written in a unified single-field form under the Boussinesq approximation. To nondimensionalize the governing equations, we introduce the following scalings for the spatial coordinate $\boldsymbol{x}$, velocity $\boldsymbol{u}$, time t, pressure p, fluid density ρ_f, and viscosity μ:

$$\tilde{\boldsymbol{x}} = \frac{\boldsymbol{x}}{R_{\text{eq}}}, \quad \tilde{\boldsymbol{u}} = \frac{\boldsymbol{u}}{U}, \quad \tilde{t} = \frac{t}{R_{\text{eq}}/U}, \quad \tilde{p} = \frac{p}{\rho_{f,0}U^2}, \quad \tilde{\rho}_f = \frac{\rho_f - \rho_{f,0}}{\gamma R_{\text{eq}}}, \quad \tilde{\mu} = \frac{\mu}{\mu_f} \tag{1}$$

where tildes denote dimensionless variables. Here, $R_{\text{eq}} = ((3/16)\, h\, [D_D^2 - d^2])^{1/3}$ is the equivalent radius of a sphere having the same volume as the disk, where D_D is the outer disk diameter, d is the diameter of the annulus, and h is the disk thickness, which is governed by the aspect ratio $\chi = D_D/h$ (see Fig. 1). The characteristic gravitational velocity scale is defined as

$$U = \sqrt{R_{\text{eq}}\, |\hat{\rho}| g}, \tag{2}$$

where $\hat{\rho}$ is defined by

$$\hat{\rho} = \frac{\rho_{f,0} - \rho_p}{\rho_{f,0}} > 0, \tag{3}$$

representing the positive relative density contrast between the reference fluid density $\rho_{f,0}$, taken at the initial disk position z_0, and the disk density ρ_p. In this work, $\hat{\rho} \approx 0.01$ is kept constant across all cases, similarly to the experiments of Fernandes *et al.* [19]. This choice of $\hat{\rho}$ is representative of microplastics in the ocean, for which the particle density is often close to that of the surrounding seawater [24]. The unperturbed background fluid density profile is assumed linear,

$$\rho_f(z) = \rho_{f,0} + \gamma z, \tag{4}$$

where $\gamma = d\rho_f/dz < 0$ is the constant density gradient within the computational domain.

The smoothed three-dimensional Heaviside function $\mathcal{H}_p(\boldsymbol{x}, t)$ takes the value 1 inside the solid and 0 in the surrounding fluid. The sharp interface between the two phases is resolved numerically with a steep, yet smooth transition across three to four grid cells [25,26]. The corresponding

TABLE I. Definitions of the dimensionless parameters used in this study. Here, V_t is the terminal velocity in a homogeneous fluid, V_z is the instantaneous vertical velocity, $\rho_f(z)$ is the local unperturbed fluid density, and $\nu = \mu_f/\rho_{f,0}$.

Name	Symbol	Definition
Disk aspect ratio	χ	$\frac{D_D}{h}$
Relative density difference	$\hat{\rho}$	$\frac{\rho_{f,0}-\rho_p}{\rho_{f,0}}$
Dimensionless moment of inertia	I^*	$\frac{1}{64}\,\frac{\rho_p}{\rho_{f,0}}\,\pi\,\frac{h}{D_D}\left(1-\frac{d^4}{D_D^4}+\frac{4}{3}\,\frac{h^2}{D_D^2}\left(1-\frac{d^2}{D_D^2}\right)\right)$
Archimedes number	Ar	$\frac{R_{\mathrm{eq}}U}{\nu}$
Froude number	Fr	$\frac{U}{NR_{\mathrm{eq}}}$
Schmidt number	Sc	$\frac{\nu}{\mathcal{D}}$
Reynolds number	Re	$\frac{V_t\sqrt{D_D^2-d^2}}{\nu}$
Instantaneous Reynolds number	Re(z)	$\frac{\lvert V_z\rvert\sqrt{D_D^2-d^2}}{\nu}$
Instantaneous Froude number	Fr(z)	$\frac{\lvert V_z\rvert}{N\sqrt{D_D^2-d^2}}$
Instantaneous Archimedes number	Ar(z)	$\sqrt{\frac{3}{16}}\,\frac{\sqrt{gh\lvert\frac{\rho_p}{\rho_f(z)}-1\rvert}\sqrt{D_D^2-d^2}}{\nu}$

dimensionless mixture density (excluding the stratification contribution) is then

$$\tilde{\rho}_0 = (1-\mathcal{H}_p) + \frac{\rho_p}{\rho_{f,0}}\,\mathcal{H}_p = 1 - |\hat{\rho}|\,\mathcal{H}_p. \tag{5}$$

Using the above scalings, the nondimensional governing equations read

$$\tilde{\boldsymbol{\nabla}}\cdot\tilde{\boldsymbol{u}} = 0, \tag{6}$$

$$\tilde{\rho}_0\,\frac{\mathrm{D}\tilde{\boldsymbol{u}}}{\mathrm{D}\tilde{t}} = -\tilde{\boldsymbol{\nabla}}\tilde{p} + \frac{1}{\mathrm{Ar}}\,\tilde{\boldsymbol{\nabla}}\cdot\left(\tilde{\mu}\left(\tilde{\boldsymbol{\nabla}}\tilde{\boldsymbol{u}} + \tilde{\boldsymbol{\nabla}}\tilde{\boldsymbol{u}}^T\right)\right) + \mathcal{H}_p\,\boldsymbol{e}_z + \frac{1}{\mathrm{Fr}^2}\,\tilde{\rho}_f\,(1-\mathcal{H}_p)\,\boldsymbol{e}_z + \tilde{\boldsymbol{F}}_{\mathrm{fsi}}, \tag{7}$$

$$\frac{\mathrm{D}\tilde{\rho}_f}{\mathrm{D}\tilde{t}} = \frac{1}{\mathrm{Ar}\,\mathrm{Sc}}\,\tilde{\boldsymbol{\nabla}}^2\tilde{\rho}_f, \tag{8}$$

where $\mathrm{D}/\mathrm{D}\tilde{t} = \partial/\partial\tilde{t} + \tilde{\boldsymbol{u}}\cdot\tilde{\boldsymbol{\nabla}}$ is the material derivative, $\boldsymbol{e}_z$ is the unit vector in the vertical direction, and $\tilde{\boldsymbol{F}}_{\mathrm{fsi}}$ denotes the nondimensional fluid-structure interaction force, implemented using a direct-forcing method [27] to impose the rigid-body velocity field inside the solid region. The hydrostatic pressure component $-R_{\mathrm{eq}}g\boldsymbol{e}_z/U^2$ is incorporated within the pressure gradient term.

The dimensionless groups (summarized in Table I) that appear in Eqs. (6)–(8) are the Archimedes, Froude, and Schmidt numbers, defined as

$$\mathrm{Ar} = \frac{R_{\mathrm{eq}}\,U\,\rho_{f,0}}{\mu_f}, \quad \mathrm{Fr} = \frac{U}{NR_{\mathrm{eq}}}, \quad \mathrm{Sc} = \frac{\mu_f}{\rho_{f,0}\mathcal{D}}, \tag{9}$$

where μ_f is the constant fluid dynamic viscosity, $\mathcal{D}$ is the molecular diffusivity of the stratifying agent, and N is the buoyancy frequency defined by

$$N^2 = -\frac{g}{\rho_{f,0}}\,\gamma. \tag{10}$$

The Archimedes number is utilized rather than the Reynolds number as the rising velocity of the disk is not known *a priori*, and the Reynolds number herein is defined as $\mathrm{Re} = \sqrt{D_D^2 - d^2}V_t\rho_{f,0}/\mu_f$, where V_t is the terminal velocity as determined from the simulations.

In nondimensional form, using $\rho_{f,0}$ and μ_f as reference scales for density and viscosity, the mixture density and viscosity fields are

$$\tilde{\rho}(\tilde{\mathbf{x}}, \tilde{t}) = \frac{\rho_f(\boldsymbol{x}, t)}{\rho_{f,0}} [1 - \mathcal{H}_p(\tilde{\mathbf{x}}, \tilde{t})] + \frac{\rho_p}{\rho_{f,0}} \mathcal{H}_p(\tilde{\mathbf{x}}, \tilde{t}), \tag{11}$$

$$\tilde{\mu}(\tilde{\mathbf{x}}, \tilde{t}) = [1 - \mathcal{H}_p(\tilde{\mathbf{x}}, \tilde{t})] + \frac{\mu_p}{\mu_f} \mathcal{H}_p(\tilde{\mathbf{x}}, \tilde{t}). \tag{12}$$

To track the motion of the rigid particle within our numerical framework, we use a signed distance function ϕ_s that measures the distance to the nearest solid–fluid interface. At the start of the simulation, we compute the initial field ϕ_s^0 at the Eulerian cell centers (x_i^0, y_i^0, z_i^0) using the known analytic description of the particle shape. At later times, the field ϕ_s^n at (x_i^n, y_i^n, z_i^n) is obtained by updating the position and orientation of the solid. The rigid-body motion is described by mass-averaged translational and rotational velocities,

$$m_p \mathbf{u}_p = \int_{\mathcal{V}} \rho_p \mathbf{u} \, d\mathcal{V}, \tag{13}$$

$$\mathbf{I}_p \boldsymbol{\omega}_p = \int_{\mathcal{V}} \mathbf{r} \times \rho_p \mathbf{u} \, d\mathcal{V}, \tag{14}$$

where m_p is the particle mass, $\mathbf{u}_p$ is the translational velocity of its centroid, $\mathcal{V}$ is the particle volume, $\mathbf{r}$ is the position vector measured from the particle center, $\mathbf{I}_p$ is the moment of inertia, and $\boldsymbol{\omega}_p$ is the angular velocity. The rigid-body velocity field inside the particle is then

$$\mathbf{u}_s(x, y, z) = \mathbf{u}_p + \boldsymbol{\omega}_p \times \mathbf{r}. \tag{15}$$

Using Eq. (15), the distance function at a current grid point (x_i^n, y_i^n, z_i^n) is obtained by tracing this point backward along the rigid-body motion to its initial position (x_i^0, y_i^0, z_i^0):

$$\phi_s(x^n, y^n, z^n) = \phi_s(x^n - u_s \Delta t,\ y^n - v_s \Delta t,\ z^n - w_s \Delta t) = \phi_s(x^0, y^0, z^0), \tag{16}$$

where $\mathbf{u}_s = (u_s, v_s, w_s)$ is defined by Eq. (15). The current signed-distance field is obtained by tracing each spatial point back to the initial particle configuration using the tracked centroid position and rotation about the three coordinate axes. Since the initial particle geometry is known analytically, its distance function can be evaluated accurately. At each time step, we evaluate this initial analytic distance function at the mapped coordinates to obtain the current signed-distance field.

Rigid-body constraints are imposed in the solid region using the momentum-averaged translational and rotational velocities. Inside the solid, we overwrite the velocity field with the rigid-body velocity given by Eq. (15) for the entire simulation, which explicitly imposes a no-slip condition on the particle. The flow in all phases is solved using a one-fluid formulation, so the resulting velocity field may not automatically satisfy no-slip at the particle surface. To enforce this, we assign a large viscosity to the solid region. In practice, a viscosity about 100 times that of the fluid is sufficient; in this work, we use a solid viscosity 500 times the fluid viscosity. A no-flux boundary condition is also imposed on the solid surface, consistent with previous studies of flow past solids in stratified fluids [4,13,28–30]. It is worth noting that the no-flux boundary condition on the solid surface is an idealized assumption in the case of temperature driven stratification, whereas it is accurate for the case of salinity-driven stratification.

The numerical method used in this work has been described in detail and extensively validated in previous studies [14,25,31]; for completeness, we provide a brief summary here. The field equations are discretized using a finite-difference method on a fixed, uniform Eulerian grid. Most spatial derivatives are approximated with second-order centered differences on a staggered grid, whereas the nonlinear convective terms are treated with a second-order essentially nonoscillatory scheme. Time advancement follows Chorin's projection method: An intermediate velocity field is first obtained by integrating the advection, viscous and body-force terms, after which an elliptic pressure Poisson equation is solved using a multigrid iterative solver and the velocity is projected

onto a divergence-free field. Temporal discretization is based on a second-order Gear method with implicit treatment of the diffusive terms, and the time step is chosen adaptively as the minimum of convective ($\Delta t_{CFL} = 0.1$) and viscous timescale constraints.

B. Simulation setup

We solve the governing equations in a three-dimensional Cartesian box of size $L_x \times L_y \times L_z = 9D_D \times 9D_D \times 48D_D$. The domain is decomposed into parallel subdomains, each covered by a uniform 64^3 finite-difference grid. The global mesh therefore contains $384 \times 384 \times 2048$ points, corresponding to a spatial resolution of $D_D/\Delta x = 42.67$. This resolution was verified to be sufficient to resolve both the disk rising dynamics and the transient jet structures. Periodic boundary conditions are imposed on the lateral boundaries, while the top and bottom boundaries satisfy free-slip, no-penetration conditions. In this work, we consider a disk aspect ratio $\chi = 7$, unless otherwise stated. This aspect ratio is chosen to be similar to previous works of rising and settling disks in homogeneous and stratified fluids [10,19].

When considering the transient dynamics of rising or settling solid and annular disks, it is convenient to introduce the nondimensional moment of inertia I^* [32]:

$$I^* = \frac{1}{64}\,\frac{\rho_p}{\rho_{f,0}}\,\pi\,\frac{h}{D_D}\left(1 - \frac{d^4}{D_D^4} + \frac{4}{3}\frac{h^2}{D_D^2}\left(1 - \frac{d^2}{D_D^2}\right)\right), \tag{17}$$

which characterizes the resistance of the disk to rotation about its centroid. One possible strategy for comparing rigid and annular disks is to enforce the same value of I^* between configurations, in addition to fixing the Archimedes and Froude numbers. This would, however, generally require adjusting the disk aspect ratio $\chi = D_D/h$, which may have a nontrivial influence on the hydrodynamic response for moderately thick disks [33]. In the present work, we therefore adopt a different approach: For a given aspect ratio, we fix the total mass of the disk and vary D_D when switching between rigid and annular geometries, so removing material from the center does not change the overall mass. With this choice, the corresponding variation in I^* remains modest; when d/D_D is varied from 0 to 0.5, I^* changes by less than 7%, which we consider acceptable for the comparisons reported below [23].

In addition, it is important to ensure that the near-surface flow is adequately resolved in our simulations. In a stratified fluid, a density boundary layer develops together with the velocity boundary layer. Resolving the near-surface density boundary layer is essential because it controls the local density gradients and hence the stratification-induced forces and torques acting on the particle. Classical boundary layer theory predicts that its thickness scales as $\delta_\rho \sim \mathcal{O}(1/\sqrt{\mathrm{Re\,Sc}})$; however, this estimate may not be directly applicable to the moderate Reynolds numbers considered here [4]. Torres *et al.* [30] indicated that, at moderate Reynolds numbers, the density boundary layer can be up to four times thicker than this classical estimate. Moreover, at intermediate Froude and Reynolds numbers, Inman *et al.* [34] reported a scaling of the form $\delta_\rho \sim \mathcal{O}(1/(\mathrm{Re\,Sc})^{1/3})$. Motivated by these observations, and to ensure adequate resolution of the density boundary layer for all configurations considered, we set the Schmidt number to $\mathrm{Sc} = 0.7$ or $\mathrm{Sc} = 7$, following More *et al.* [13]. These values are representative of a thermally stratified atmosphere and of water, respectively. With this choice, the density boundary layer is resolved by at least a few grid points across the range of Reynolds and Froude numbers examined in this study.

Lastly, in this work, the disk is released from a vertical position of $2D_D$ from the bottom of the domain, with an initial inclination $\theta_0 = 5^\circ$, where θ is defined in Fig. 1. Previous studies have typically adopted similar initial angles, $\theta_0 \in [0^\circ,\ 10^\circ]$ [10,35]. Nevertheless, previous work indicates that long-term dynamics is independent of initial inclination, both in homogeneous conditions [36] and in a density-stratified environment [10].

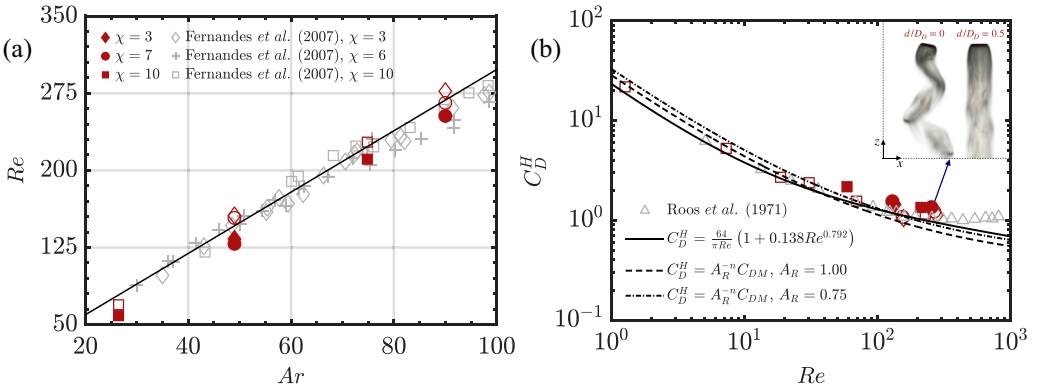


FIG. 2. (a) Reynolds number as a function of the Archimedes number for rising disks in a homogeneous fluid. The computational results are presented against the experimental results of Fernandes *et al.* [19] for various aspect ratios χ. The solid line corresponds to $C_D^H = 1.2$. (b) Comparison of the drag coefficient C_D^H from the simulations to empirical correlations and experimental measurements [37]. The inset shows two sample volume renderings of the vorticity profile for an impervious and perforated disk with $d/D_D = 0.5$ (Ar = 90, $\chi = 7$). The open red symbols correspond to the simulation results with solid disks, and the filled red symbols correspond to perforated disks with $d/D_D = 0.5$.

III. RESULTS AND DISCUSSION

The following subsections present simulation results for disks rising in (i) a homogeneous fluid and (ii) a density-stratified fluid, with the objective of isolating the influence of a central perforation on the disk dynamics. We examine how the perforation modifies key features of the motion, including the rise velocity, trajectory, and inclination angle, and the associated wake structure relative to an impervious disk. Throughout, the trends observed in the simulations are compared against relevant experimental and numerical results available in the literature to place the present findings in context and to validate the observed computational results.

A. Rising disk dynamics in a homogeneous ambient

We begin our discussion by comparing our numerical results for unperforated disks with the experiments of Fernandes *et al.* [19]. Figure 2 shows the Reynolds numbers, calculated from the mean rising velocity once the disks have reached steady state behavior in a homogeneous fluid, as a function of the Archimedes number. The open symbols in Fig. 2 correspond to unperforated disks, whereas filled symbols correspond to perforated disks with $d/D_D = 0.5$. The plots include simulation results for disk aspect ratios ranging from $\chi = 3$ to $\chi = 10$.

The slope obtained from the data plotted in Fig. 2(a) is typically used to determine the drag coefficient (C_D^H) of rising or settling objects. In a homogeneous fluid, the drag coefficient can be extracted under the assumption of steady state behavior, once the disk has reached a terminal velocity. In steady state, the net buoyancy force, $(\rho_{f,0} - \rho_p)gV_p$, which is constant in time for a homogeneous fluid, is balanced by the hydrodynamic drag along the vertical direction. Assuming rising or settling with a broadside-on orientation, this balance gives

$$(\rho_{f,0} - \rho_p)gV_p = \tfrac{1}{2}\rho_{f,0} C_D^H V_t^2 A_s, \tag{18}$$

where $V_p = \pi(D_D^2 - d^2)h/4$ is the volume of the disk and $A_s = \pi(D_D^2 - d^2)/4$ is the solid area. The drag coefficient can then be readily extracted as $C_D^H = 2|\hat{\rho}|hg/V_t^2$. To relate Eq. (18) to Fig. 2,

the Archimedes number may be rewritten as

$$\mathrm{Ar} = \sqrt{\frac{3}{16}}\frac{\rho_{f,0}\sqrt{gh|\hat{\rho}|}\sqrt{D_D^2 - d^2}}{\mu_f}. \tag{19}$$

From the definitions of the Reynolds and Archimedes numbers and Eq. (18), it follows that C_D^H can be expressed in terms of Re and Ar as

$$C_D^H = \frac{32}{3}\frac{\mathrm{Ar}^2}{\mathrm{Re}^2}. \tag{20}$$

Physically, the dependence of C_D^H on $\mathrm{Ar}^2/\mathrm{Re}^2$ arises because Ar characterizes the buoyancy forcing, while Re characterizes the resulting rise velocity, so their ratio measures the drag required to balance the buoyancy-driven motion [19]. In Fig. 2(a), the solid line corresponds to $C_D^H = 1.2$, consistent with the mean drag coefficient reported by Fernandes *et al.* [19] for rising solid disks. Their experiments covered $80 \leqslant \mathrm{Re} \leqslant 330$ and $1.5 \leqslant \chi \leqslant 20$, with a density ratio close to unity. The numerical results for the unperforated disks are consistent with this trend, whereas the perforated disks yield systematically lower Re at a given Ar (with no discernible dependence on χ), indicating a modest increase in the effective drag due to the presence of the perforation. A similar increase in the drag coefficient was found when comparing the flow around dandelion seeds with impervious disks [38], attributed to the reduced projected area of the former. The pappus generated more than 4 times the drag per unit area of an equivalent impervious disk. Furthermore, the dependence of C_D^H on χ contrasts with the behavior reported for rising spheroids at high Reynolds numbers by Will *et al.* [39], who found that C_D^H increases from approximately 0.59 for a sphere to about 2.08 for an oblate spheroid with a small aspect ratio.

Figure 2(b) compares the numerical predictions of the drag coefficient, C_D^H, as a function of the Reynolds number, Re, with two empirical correlations and the disk measurements of Roos and Willmarth [37], who experimentally measured drag coefficients for spheres and disks. Additionally, two sample volume renderings of the vorticity profile are provided in the inset for $\mathrm{Ar} = 90$, $\chi = 7$. The first correlation,

$$C_D^H = \frac{64}{\pi \mathrm{Re}}\left(1 + 0.138\,\mathrm{Re}^{0.792}\right), \tag{21}$$

is applicable to disks with $\chi > 1$ settling or rising broadside-on for $1.5 \lesssim \mathrm{Re} \lesssim 130$ [10,40]. We also consider a formulation developed for ice particles falling in air that accounts for the projected area ratio (A_R) [41,42],

$$A_R = \frac{A_s}{A}, \quad A = \frac{\pi D_D^2}{4}, \quad C_D^H = A_R^{-n} C_{DM}, \tag{22}$$

where

$$C_{DM} = C_0\left(1 + \frac{\delta_0}{\mathrm{Re}^{1/2}}\right)^2. \tag{23}$$

For the solid and annular disks in Fig. 2(b), $A_R = 1$ and $A_R = 0.75$, respectively, since $A_R = 1 - (d/D_D)^2$. Here, $n = \frac{1}{2}$, $C_0 = 0.35$, and $\delta_0 = 8$, following Heymsfield and Westbrook [41]. This formulation was also adopted by Tinklenberg *et al.* [42] in their analysis of the settling dynamics of solid and perforated disks in quiescent and turbulent air. Although originally developed for ice particles falling in air, its relevance here is therefore geometric rather than specific to the present flow regime. Overall, both correlations provide reasonable estimates of C_D^H at low Re; however, they slightly underestimate C_D^H as Re increases. The numerical results for solid disks are in excellent agreement with the measurements of Roos and Willmarth [37] over the range of Re considered.

Figure 3 shows four representative simulation cases: (a) $\mathrm{Ar} = 90$, $\chi = 7$ and (b) $\mathrm{Ar} = 49$, $\chi = 7$, each for a solid disk and a perforated disk with $d/D_D = 0.5$. The corresponding moment of inertia

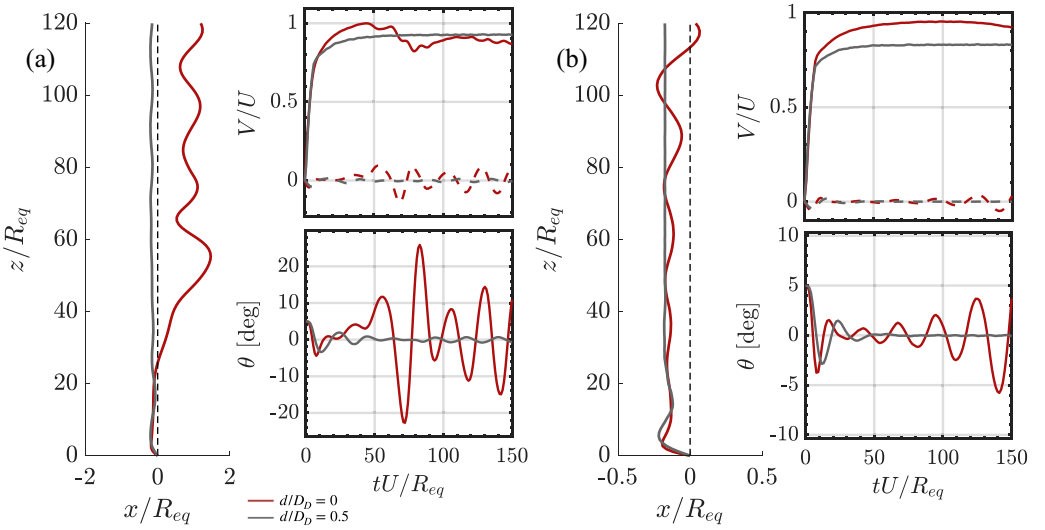


FIG. 3. Disktrajectory in the x-z plane, time histories of the vertical (V_z, solid) and lateral (V_x, dashed) velocities, and the inclination angle θ shown for Ar = 90, $\chi = 7$, and Ar = 49, $\chi = 7$ in (a) and (b), respectively. Here, $I^* = 0.0072$ for solid disks and $I^* = 0.0067$ for perforated disks.

for the solid and perforated cases are $I^* = 0.0072$ and $I^* = 0.0067$, respectively. When the disks are released from rest with a finite initial inclination angle ($\theta_0 = 5°$), they rotate to a broadside-on orientation ($\theta = 0°$) as they align to maximize the projected area normal to the direction of motion. After this initial reorientation, the side-view trajectories in the x/R_{eq}-z/R_{eq} plane indicate that the solid disks undergo a pronounced fluttering motion during ascent for both Ar considered. Furthermore, the time histories of the vertical (V_z) and lateral (V_x) velocities are shown (solid and dashed lines, respectively). For the solid disk at Ar = 90, the vertical velocity V_z exhibits weak oscillations once the initial transient associated with the disk's acceleration from rest has ended [19].

The fluttering regime is further characterized by oscillations of the disk's inclination angle. From the frequency f of these pitching oscillations, we define the Strouhal number based on the disk diameter D_D and the terminal velocity V_t as $\mathrm{St} = fD_D/V_t$. For the solid disks, we obtain St = 0.17 at Ar = 90 and St = 0.13 at Ar = 49, which is similar to previous works [19,33]. Introducing a central perforation suppresses the fluttering dynamics: The perforated disks rise along a nearly rectilinear trajectory with negligible lateral drift. This behavior is observed for both Ar = 90 and Ar = 49, as indicated by the near-zero lateral velocity V_x and the markedly reduced oscillations of the inclination angle θ after the initial transient. In addition, once the perforated disks attain their terminal velocity, the vertical velocity V_z becomes essentially steady, with no discernible oscillations. Previous experimental studies [23,35] have shown that introducing a central perforation can stabilize the motion of a disk at large Reynolds numbers. In particular, as d/D_D increases, a transition from a tumbling regime to a chaotic regime has been reported. Related regime changes have also been observed for disks with alternative perforation patterns [42] and for perforated plates [43].

Vincent *et al.* [23] reported that the stabilizing influence of a central perforation becomes apparent once the hole reaches a critical size, with the transition occurring at approximately $d/D_D \simeq 0.3 \pm 0.1$. They further found that this regime change shifts to smaller values of d/D_D as the moment of inertia I^* decreases. Relative to the regime map for solid disks compiled by Field *et al.* [21], increasing d/D_D may therefore be interpreted as effectively lowering I^* at fixed Re [23]. An additional simulation is shown in Fig. 4 for Ar = 49 and $\chi = 7$ in a homogeneous fluid, where

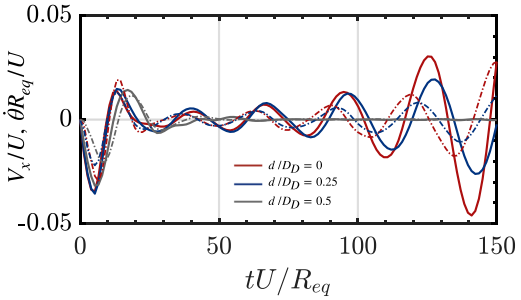


FIG. 4. Time histories of the disk lateral velocity V_x (solid lines) and angular velocity $\dot{\theta}$ (dash-dotted lines) for Ar = 49 and $\chi = 7$, with varying d/D_D. The corresponding dimensionless moments of inertia are $I^* = [0.0072,\ 0.0071,\ 0.0067]$ for $d/D_D = [0,\ 0.25,\ 0.5]$, respectively.

the area ratio is varied through d/D_D. The figure reports the time evolution of the lateral velocity component, V_x, and the angular velocity $\dot{\theta}R_{\rm eq}/U$. When the perforation is smaller ($d/D_D = 0.25$), fluttering persists with pronounced lateral oscillations, whereas for $d/D_D = 0.5$ the amplitude of V_x is strongly reduced, in agreement with the experimental observations of Vincent *et al.* [23] at high Re. We find that the phase angle, which quantifies the lag between the disk orientation and its direction of motion, is $\Delta\phi \approx 70^\circ$. This is consistent with previous measurements showing a strong dependence on aspect ratio; in particular, $\Delta\phi \gtrsim 90^\circ$ for sufficiently thin disks with $\chi \gtrsim 8$ ($\chi = 7$ in this work) [39,44,45].

When considering the flow field, Moffatt [46] posed the question of how the existence of holes may modify the wake dynamics of a disk, and, in turn, the instabilities associated with it. Recently, Zhang *et al.* [35] reported substantial differences in the wake of settling disks with multiple perforations, attributed to vortical structures shed from the holes. Here, Fig. 5 presents the temporal evolution of the vorticity field when Ar = 90, $\chi = 7$ in a homogeneous fluid. The development of the wake behind the disk is presented in the x-z plane from $tU/R_{\rm eq} = 30$ up to $tU/R_{\rm eq} = 100$ for a solid disk in Fig. 5(a) and a perforated disk with $d/D_D = 0.5$ in Fig. 5(b). A drastic difference between the wake structures is apparent in the vorticity field (ω_y). In Fig. 5(a), shear layers of opposite sign form behind the disk, and as the disk transitions to the fluttering regime after the initial transient, the wake becomes asymmetric and vortices are periodically shed downstream, with a shedding frequency comparable to that of the disk oscillation [44,47]. In contrast, Fig. 5(b) shows that vorticity is generated not only at the outer rim of the disk (as in the impervious case) but also at the rim of the central hole. This produces an additional, oppositely signed toroidal vortex in the near wake, along with the primary vortex ring attached to the outer edge. Vincent *et al.* [23] found in their high-Re experiments that the secondary counterrotating vortex ring generated at the rim of the central hole plays a key role in the observed stabilization, promoting the transition from a tumbling regime to a chaotic regime.

The role of the secondary vortex ring in the stabilization process is examined through the circulation (Γ) in Fig. 6, following Vincent *et al.* [23]. In Fig. 6(a), a closeup of the ω_y field in the x-z plane is shown for $tU/R_{\rm eq} = 30$. Streamlines in the body reference frame are also included: they highlight the primary vortex ring attached to the outer rim in the solid disk case and, for the perforated disk, the presence of both this primary vortex ring and a secondary vortex ring associated with the inner rim. Here, Γ is evaluated during the initial stage of the simulation, from $tU/R_{\rm eq} = 0$ to $tU/R_{\rm eq} = 30$, as shown in Fig. 6(b). For solid disks, the contribution to Γ is solely derived from the primary vortex ring; we denote this contribution by Γ_0, as indicated in the schematic in Fig. 6(b). For the perforated disk, both the primary and secondary vortex rings contribute to the effective circulation. Here, Γ_i denotes the circulation associated with the secondary vortex ring. Since the secondary vortex ring rotates in the opposite direction to the primary ring, the effective circulation

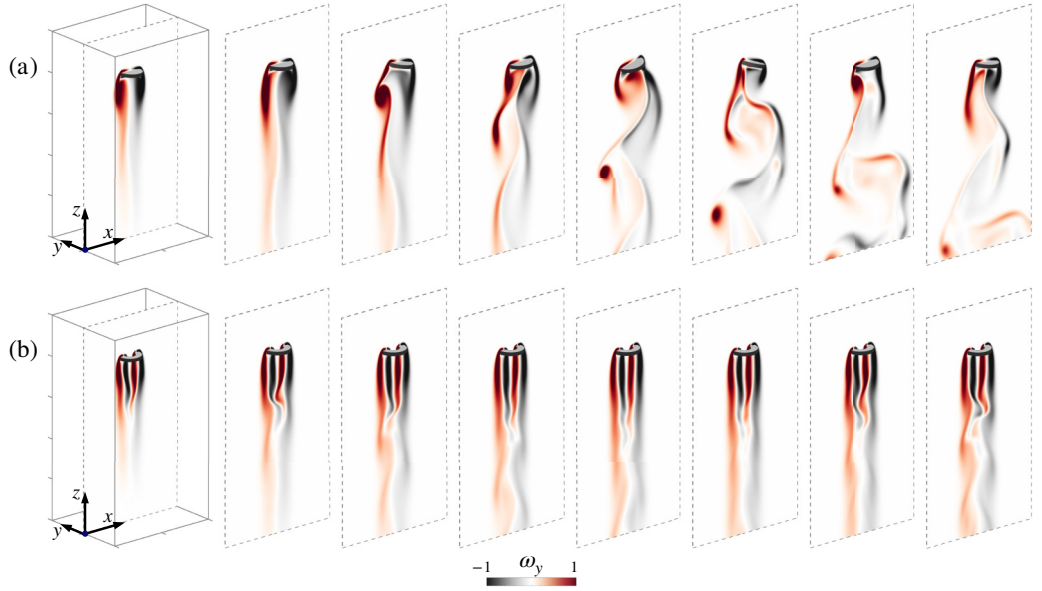


FIG. 5. Spatiotemporal evolution of the vorticity profiles ω_y in the x-z plane with Ar $= 90$, $\chi = 7$ for a solid disk in (a) and a perforated ($d/D_D = 0.5$) disk in (b). The time history spans $tU/R_{\text{eq}} = 30$ to $tU/R_{\text{eq}} = 100$, with snapshots taken at intervals of $\Delta t = 10$. The results are shown on a slice in the y–normal direction, with a height of $9D_D$, extending from $1.8D_D$ above the disk to $7.2D_D$ below the disk.

is computed as [23]

$$\Gamma = \Gamma_0 - \frac{d}{D_D}\Gamma_i. \tag{24}$$

The circulation is evaluated on a central x-z slice by integrating the y component of vorticity over the fluid region. The slice is divided into left and right halves relative to the domain centerline, and

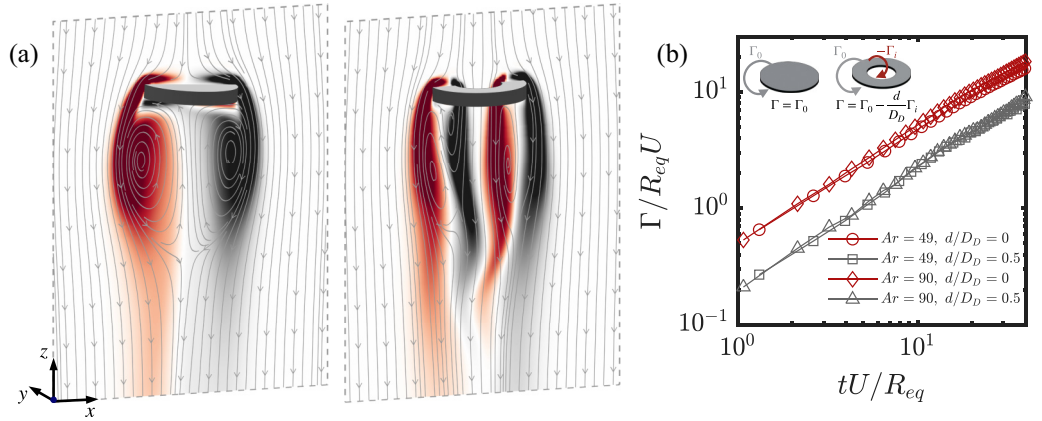


FIG. 6. (a) Close-up comparison of the vorticity profile and the body frame streamlines with Ar $= 90$, $\chi = 7$ for a solid and perforated disk ($d/D_D = 0.5$) at $tU/R_{\text{eq}} = 30$. The color map is the same as Fig. 5. The time history of the circulation Γ is presented in panel (b), where the inset illustrates the contributions to Γ for either case.

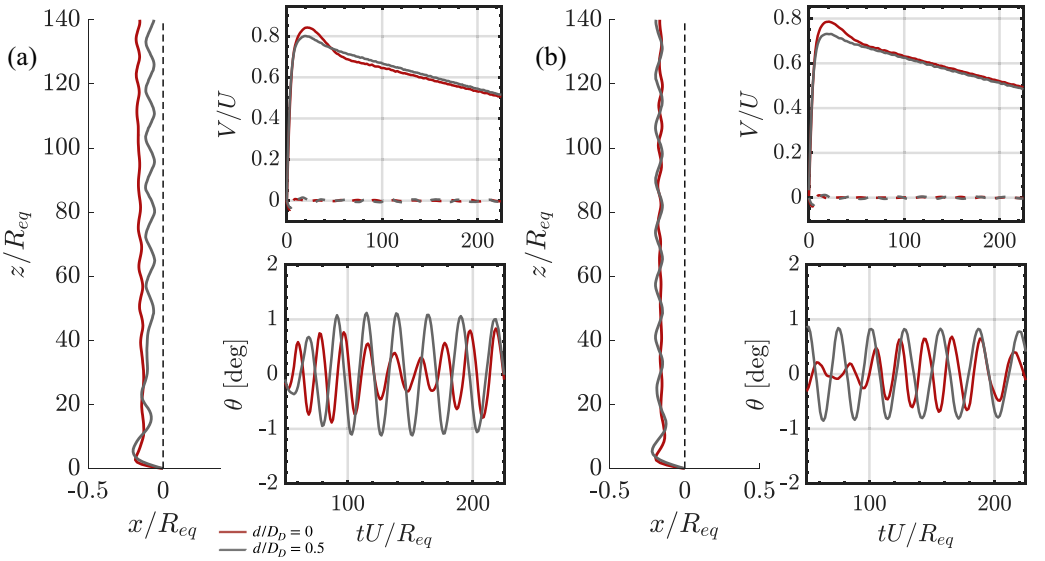


FIG. 7. Disktrajectory in the x-z plane, time histories of the vertical (V_z, solid) and lateral (V_x, dashed) velocities, and the inclination angle θ for Ar = 90, $\chi = 7$, Fr = 17, Sc = 0.7, and Ar = 49, $\chi = 7$, Fr = 17, Sc = 0.7 shown in (a) and (b), respectively. Here, $I^* = 0.0072$ for solid disks, and $I^* = 0.0067$ for perforated disks.

positive and negative vorticity regions are treated separately. Weak background vorticity is excluded by retaining only connected regions whose vorticity exceeds a small fraction of the local peak magnitude on each side. For the impervious disk, the reported circulation is obtained by averaging the absolute contributions from the dominant vortex regions. In Fig. 6(b), the circulation for the solid disks collapses onto a single curve for both Ar = 49 and Ar = 90, while the perforated disks exhibit a lower circulation. The lower effective circulation is consistent with the opposing contribution of the inner-rim vortex ring and the observed stabilization of the annular disk.

B. Rising disk dynamics in a density-stratified ambient

Introducing background stratification adds additional complexities that are absent in a homogeneous environment. In a homogeneous fluid, a rising disk often approaches a terminal rise velocity and statistically steady behavior after an initial transient. On the other hand, dynamics remain height-dependent in a density-stratified fluid because the buoyancy force varies with the local fluid density $\rho_f(z)$. As a result, the disk may exhibit quasisteady behavior over limited vertical intervals [10], but its rise velocity can continue to evolve as it ascends.

Stratification influences not only the vertical velocity but also the lateral drift and the inclination angle. Figure 7 shows the side view (x-z plane), the vertical and lateral velocity components (V_z and V_x), and the inclination angle (θ) for four representative simulations when Fr = 17, Sc = 0.7, $\chi = 7$. Figure 7(a) corresponds to Ar = 90, and Fig. 7(b) corresponds to Ar = 49. Two main observations are made when comparing the disk dynamics in a density-stratified ambient and a homogeneous fluid. All four representative simulations show that as the disk rises, it attains a maximum rise velocity after the initial transient, followed by a monotonic decrease in the rising velocity. This behavior has been observed previously for settling spheres [4], spheroids [13,31], and impervious disks [10] in a linearly stratified fluid. Moreover, the oscillation amplitudes of the inclination angle ($\simeq \pm 1^\circ$) and the lateral displacement are notably reduced relative to the homogeneous fluid cases for impervious disks. When perforated disks are considered, the peak velocity attained by the disk is slightly lower than that of a solid disk. This is attributed to the

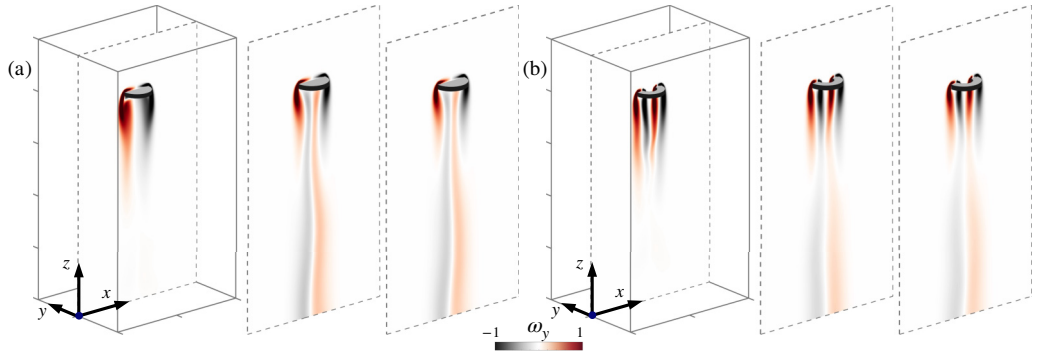


FIG. 8. Spatiotemporal evolution of the vorticity profiles ω_y in the x-z plane with Ar = 90, $\chi = 7$, Fr = 17, Sc = 0.7 for a solid disk in (a) and a perforated ($d/D_D = 0.5$) disk in (b). The time history spans $tU/R_{\text{eq}} = 30$ to $tU/R_{\text{eq}} = 150$, with snapshots taken at intervals of $\Delta t = 60$. The results are shown on a slice in the y–normal direction, with a height of $9D_D$, extending from $1.8D_D$ above the disk to $7.2D_D$ below the disk.

reduced perturbation of local ambient stratification due to the presence of the hole, and the effect of which on the wake is presented in Figs. 8 and 9 for Ar = 90. In representative simulations, the oscillations of the inclination angle may also be influenced by the background stratification. However, the present parameter regime (moderate Fr) does not allow a clear separation between the intrinsic body oscillation of the disk and the stratification effects associated with the buoyancy frequency N [10].

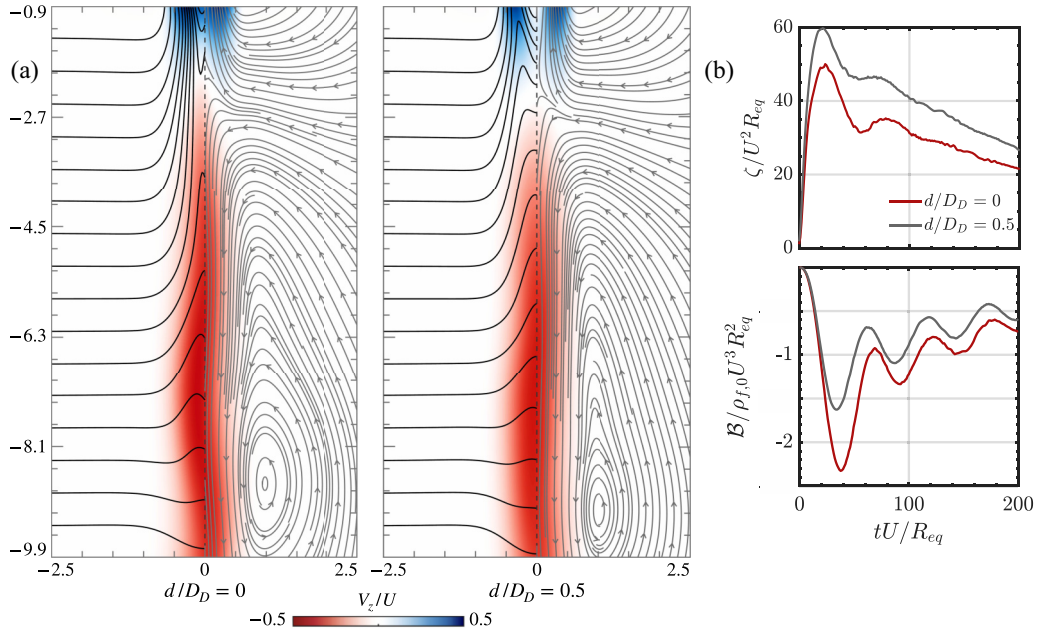


FIG. 9. (a) Side views in the x-z plane of the wakes for a solid disk and a perforated disk with $d/D_D = 0.5$ in the stratified cases at Ar = 90, $\chi = 7$, Fr = 17, and Sc = 0.7 at $tU/R_{\text{eq}} = 150$. The axes are normalized by D_D and are with respect to the center of mass of the disk. The left side presents the distorted isopycnals, and the right side shows the laboratory frame streamlines. (b) Temporal evolution of the enstrophy ζ, and the buoyancy flux $\mathcal{B}$.

By taking the curl of the momentum equation, the vorticity equation can be derived for density-stratified fluids under the Boussinesq approximation [1]:

$$\frac{\mathrm{D}\boldsymbol{\omega}}{\mathrm{D}t} = (\boldsymbol{\omega}\cdot\boldsymbol{\nabla})\boldsymbol{u} + \nu\nabla^2\boldsymbol{\omega} - \frac{g}{\rho_{f,0}}\boldsymbol{\nabla}\rho_f \times \boldsymbol{e}_z, \tag{25}$$

where ν is the kinematic viscosity. In a density-stratified fluid, the last term on the right-hand side of Eq. (25) represents baroclinic vorticity generation arising from the local misalignment between the density gradient and the vertical direction. Note that under the Boussinesq approximation, the baroclinic source term includes the hydrostatic contribution alone, compared to the usual term proportional to $\boldsymbol{\nabla}\rho_f \times \boldsymbol{\nabla}p$. In the present context, this term becomes significant when the rising disk distorts the ambient density field and the associated isopycnals.

Figure 8 presents the temporal evolution of the disk rise at three different time steps for an impervious disk in panel (a) and a perforated disk in panel (b) ($\mathrm{Ar} = 90,\ \chi = 7,\ \mathrm{Fr} = 17,\ \mathrm{Sc} = 0.7$).

As the solid disk rises from rest, a primary vortex ring forms near the disk surface. The disk distorts the ambient density field, which promotes baroclinic vorticity generation, leading to the formation of a buoyancy induced secondary toroidal vortex of opposite sign in the downstream wake [4,13,31,48]. When the perforated disk rises, it initially forms a pair of counterrotating vortices near the disk outer and inner edges. After some time, a toroidal vortex of opposite sign to the primary vortex ring develops downstream, in a manner similar to the solid disk case.

To further characterize the wake dynamics in a density-stratified fluid, the velocity field downstream of the disk is presented in Fig. 9 at $tU/R_{\mathrm{eq}} = 150$ in the x-z plane. Figure 9(a) shows the wake of the solid and perforated disk, with the associated isopycnals on the left and the laboratory-frame streamlines on the right. The axes are normalized by D_D and are with respect to the center of mass of the disk. For a sphere moving vertically at a constant speed in a density-stratified fluid, Torres *et al.* [30] found complete collapse of the rear vortex with increasing stratification strength (decreasing Fr). However, that does not mean the flow is irrotational, as can be seen from the laboratory frame streamlines, where a region of large vorticity exists in the wake of the disk. A region of positive velocity is observed near the disk surface in both the impervious and perforated cases, associated with the disk rise. The isopycnals are distorted in the near wake, and as they return toward their neutrally buoyant position, a region of negative velocity develops downstream of the disk. Furthermore, comparing the distorted isopycnals in the solid and perforated cases reveals that, immediately downstream of the disk, there is a region of reduced isopycnal displacement for the perforated disk case.

Figure 9(b) shows the time histories of the enstrophy (ζ) and the volume-integrated buoyancy flux ($\mathcal{B}$). In a density-stratified fluid, the buoyancy flux quantifies the reversible exchange between kinetic and potential energy [49] and is linked to baroclinic vorticity production. These quantities are defined as

$$\zeta = \frac{1}{2}\int_V \|\boldsymbol{\omega}\|^2\, dV, \tag{26}$$

$$\mathcal{B} = -g\int_V V_z^f \rho_f'\, \mathrm{d}V. \tag{27}$$

Here, V denotes the fluid region throughout the computational domain, excluding the solid particle, and ρ_f' is the departure from the unperturbed linear density profile at the same height. The squared vorticity magnitude is $\|\boldsymbol{\omega}\|^2 = \boldsymbol{\omega}\cdot\boldsymbol{\omega}$. Comparing the buoyancy flux between the solid and perforated disks reveals that $|\mathcal{B}|$ is larger for the solid disk. This indicates a stronger generation of baroclinic vorticity in the solid disk wake, consistent with the larger perturbation of the ambient density field (more exchange from kinetic to potential energy). However, enstrophy, which measures the intensity of rotational flow, is larger at all times when $d/D_D = 0.5$, attributed to the vorticity produced near the disk hole.

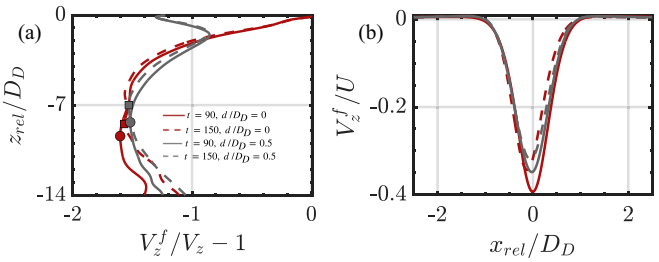


FIG. 10. (a) Centerline profile of the relative wake vertical velocity $V_z^f/V_z - 1$ as a function of z_{rel}, the vertical coordinate measured relative to the disk center at its instantaneous height for Ar $= 90$, $\chi = 7$, Fr $= 17$, and Sc $= 0.7$ at $tU/R_{\text{eq}} = 90$ and $tU/R_{\text{eq}} = 150$. Symbols indicate the relative vertical position z_{rel} at which V_z^f attains its minimum. Circles correspond to $tU/R_{\text{eq}} = 90$, and squares correspond to $tU/R_{\text{eq}} = 150$. (b) Lateral profile of V_z^f/U along the x direction evaluated at these marker locations.

In Fig. 10(a), the relative velocity of the fluid $(V_z^f/V_z - 1)$ along the centerline of the wake is presented at two different time steps when Ar $= 90$, Fr $= 17$, Sc $= 0.7$, where the symbols represent the axial positions of the maximum $|V_z^f|$. In Fig. 10(b), a transverse plot along the region indicated by the symbols of Fig. 10(a) is presented. Figure 10(b) shows that the maximum fluid velocity magnitude in the caudal (jet) region of the disk wake is smaller when a perforation is introduced into the disk, consistent with the observations made in Fig. 9. A standing eddy, which corresponds to a relative velocity $(V_z^f/V_z - 1)$ greater than zero near the disk surface (close to $z_{\text{rel}} = 0$) for the impervious disk, is not found for Ar $= 90$. Similarly, Zhang *et al.* [6] found no standing eddy behind a sphere settling at a constant speed at Re $= 100$ throughout their investigated range $0.1 \leqslant \text{Fr} \leqslant 10$. When $d/D_D = 0.5$, a region of downward axial velocity is observed in the near wake, immediately adjacent to the disk. This behavior is a direct consequence of flow through the central aperture. As the disk rises, a pressure difference between the upstream and downstream faces drives a localized flow through this aperture. The resulting flow through the perforation introduces downward momentum into the wake in the immediate vicinity of the disk, yielding negative V_z^f along the wake centerline. In the disk frame, this manifests as a relative velocity $(V_z^f/V_z - 1) < -1$ near $z_{\text{rel}} \approx 0$ compared with the impervious disk. From Fig. 10(a), it can be seen that the stratification induced localized jet downstream of the disk is slightly shorter when introducing the perforation. A similar behavior is found in Fig. 11 when comparing the flow field when Ar $= 49$ at $tU/R_{\text{eq}} = 150$, where panel (a) corresponds to (Sc $= 0.7$, Fr $= 17$), panel (b) to (Sc $= 7$, Fr $= 17$) and panel (c) to (Sc $= 7$, Fr $= 11.4$).

When decreasing Ar while keeping (Sc, Fr) fixed, the jet region of the wake follows the same trend as in Fig. 10. However, closer to the disk surface, the impervious disk case shows a slightly positive $V_z^f/V_z - 1$, indicating that the standing eddy persists under these conditions and has not completely collapsed. This can be visualized through the body frame streamlines adjacent to the disk surface. Decreasing the diffusivity of the stratifying agent (increasing Sc) leads to a more pronounced distortion of the ambient density field, visible as stronger isopycnal deformation. The associated transverse density gradients contribute to baroclinic vorticity generation through the cross product in Eq. (25), consistent with the increased peak jet velocity magnitude. The collapse of the standing eddy is stronger when increasing Sc, and the discrepancy in the jet strength between the impervious and perforated disks becomes more pronounced, evidenced by a larger separation in the profiles of $V_z^f/V_z - 1$. When decreasing Fr, Fig. 11(c) shows the complete collapse of the standing eddy, as seen by Torres *et al.* [30] when decreasing Fr. Decreasing Fr leads to an increase in the potential energy attained by the fluid parts, so that the exchange between the fluid potential and the kinetic energy is stronger. As a result, the strength of the jet intensifies as Fr decreases, as seen both in the velocity field and in the centerline profile of the relative velocity. The disparity

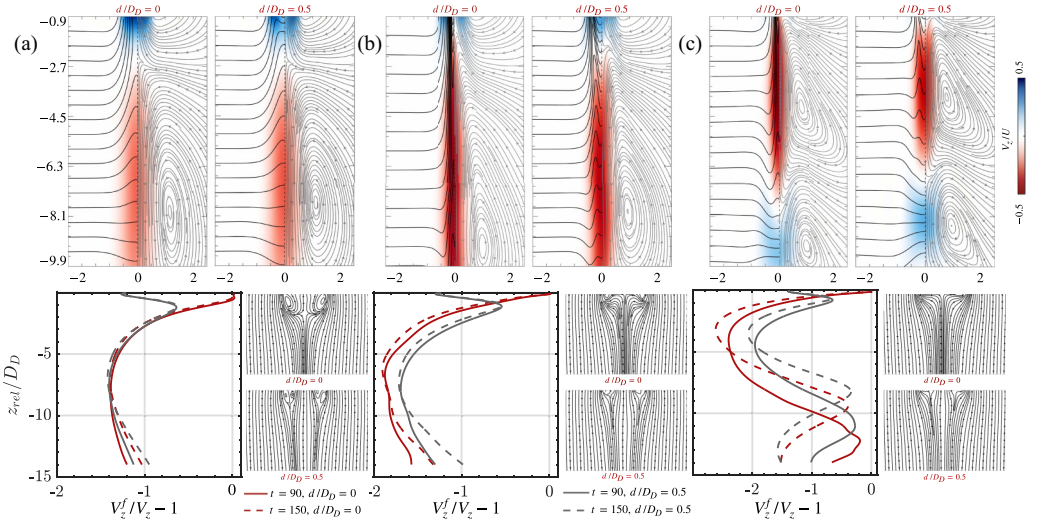


FIG. 11. (a) Side views in the x-z plane of the wakes for a solid disk and a perforated disk with $d/D_D = 0.5$ in the stratified cases at Ar $= 49$, $\chi = 7$, Fr $= 17$, and Sc $= 0.7$ at $tU/R_{\text{eq}} = 150$. The axes are normalized by D_D and are with respect to the center of mass of the disk. The left side presents the distorted isopycnals, and the right side shows the laboratory frame streamlines. The body frame streamlines are presented at $tU/R_{\text{eq}} = 150$, and a plot of the relative fluid velocity $V_z^f/V_z - 1$ is presented at two different time steps. (b) and (c) correspond to (Sc $= 7$, Fr $= 17$) and (Sc $= 7$, Fr $= 11.4$), respectively.

between impervious and perforated cases also grows, affecting both the jet length and its associated velocity profile.

The effect of varying Sc is considerable when visualizing the wakes in Figs. 11(a) and 11(b). However, the influence of stratification on the disk rising dynamics is rooted in the fluid buoyancy force, which, if left constant, leads to similar behavior, as observed in Fig. 12(a). For both oblate and prolate spheroids, More *et al.* [13] likewise found only modest changes in the settling velocity histories when increasing Sc (denoted Pr in their paper) from 0.7 to 7. However, for settling spheres or

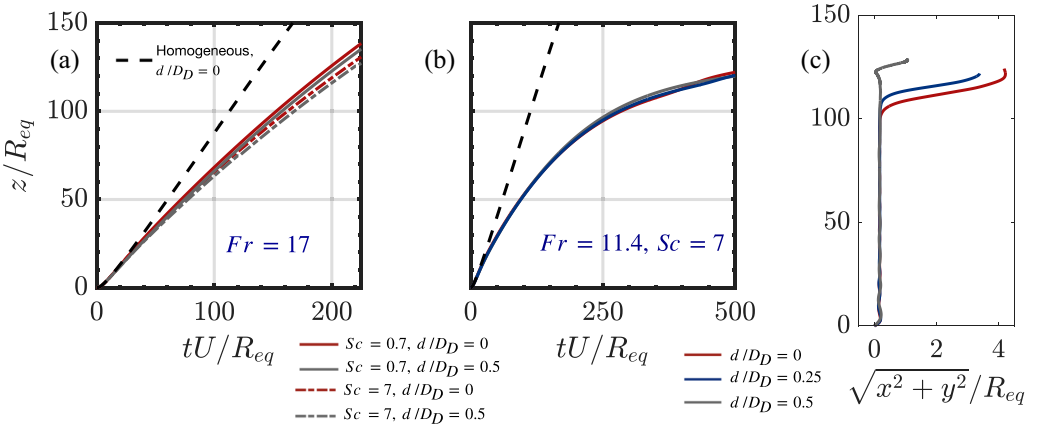


FIG. 12. Time histories of the disk's instantaneous vertical position are shown for (a) Ar $= 49$ at Fr $=$ 17 with Sc $= 0.7$ and Sc $= 7$ for both $d/D_D = 0$ and $d/D_D = 0.5$, and (b) Ar $= 49$, Sc $= 7$, Fr $= 11.4$ for $d/D_D = 0$, 0.25, and 0.5. (c) Corresponding rise trajectories for the cases in (b).

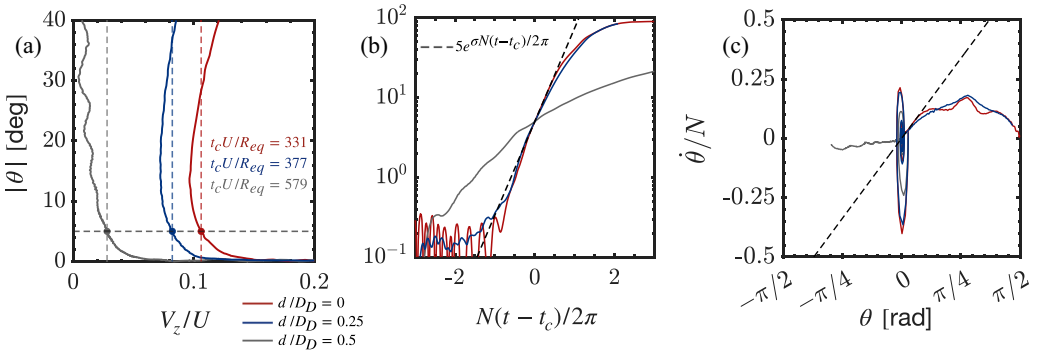


FIG. 13. (a), (b) Time history of $|\theta|$ with respect to V_z/U and $N(t-t_c)/2\pi$, respectively. Here t_c is the time where $\theta = 5^\circ$ during the reorientation process. The dashed line in (b) corresponds to $5e^{\sigma N(t-t_c)/2\pi}$, where $\sigma = 2.7$ as per the experiments of Mercier *et al.* [10]. In (c), the phase diagram of the angular velocity and the orientation angle is presented, where the dashed line has a slope of $\sigma/2\pi$. The results here correspond to $\mathrm{Ar} = 49,\ \mathrm{Sc} = 7,\ \mathrm{Fr} = 11.4$ and varying d/D_D.

rising droplets, the vertical velocity oscillation with an oscillation frequency related to N was found in strongly stratified fluids. The Schmidt number affects these oscillations through the evolution of the displaced ambient density field. Increasing Sc reduces density diffusion, allowing the entrained fluid to retain its density contrast for longer and potentially modifying the stratification-induced drag and reorientation dynamics.

When increasing the stratification strength, the disk rises with heavier fluid surrounding the disk surface into a position of lighter fluid. In turn, the increased deceleration of the disk associated with the increase in fluid buoyancy force can be seen in Fig. 12(b), which presents the instantaneous vertical position of the disk when varying d/D_D. Furthermore, disks and spheroids have been shown to reorient from the stable broadside-on configuration observed in a homogeneous fluid to an edgewise configuration when the stratification is sufficiently strong. Here, an edgewise orientation denotes a configuration in which the disk presents a minimal projected area to the direction of motion, denoted by $\theta = 90^\circ$. The change in stability that governs the reorientation of disks and spheroids in linearly stratified fluids has previously been reported to occur after the magnitude of the particle velocity drops below a certain threshold. The reorientation of the particle is associated with the dominance of buoyancy induced torque over the hydrodynamic torque. More *et al.* [13] found that the threshold velocity required for spheroids to reorient depends on the Galilei and Richardson numbers (Ar and Fr in this work). Moreover, the process of reorientation is accompanied by lateral (in-plane) drift, prior to the particle reaching its neutrally buoyant position. This is observed when considering Fig. 12(c) after the initial broadside-on rising phase. Figure 12(c) further shows that the onset of lateral drift varies when increasing d/D_D, such that the disk reaches a higher vertical position, where the ambient fluid density is lower, with a broadside-on orientation.

The corresponding orientation dynamics are presented in Fig. 13, showing how the aperture affects the onset and subsequent growth of reorientation. The time at the onset of reorientation (here taken at $\theta = 5^\circ$ after the broadside rising phase) in Fig. 13 is denoted by t_c. A clear trend can be seen, where t_c increases with increasing aperture ratio d/D_D, indicating that the broadside regime becomes more stable as the disk tends toward the shape of a thin ring (increasing d/D_D). Figure 13(a) shows that as t_c increases with increasing d/D_D, the threshold velocity required for the reorientation process decreases. Although outside the scope of the current work, it would be interesting to consider the role of different styles of perforations on the onset or suppression of the reorientation process in a density-stratified ambient.

In Figs. 13(b) and 13(c), the temporal evolution of the magnitude of θ and the phase diagram of the angular velocity with respect to the orientation angle are presented. From simulations and

experiments of Mercier *et al*. [10] for solid disks settling in a linearly stratified environment, it was shown that as the disk settles, there is a convergence toward $(\theta, \dot{\theta}) = (0, 0)$ prior to the start of reorientation. A similar convergence can be seen here during the broadside-on rising phase, attributed to the suppression of flutter induced by ambient stratification [18]. Furthermore, from the experimental results of Mercier *et al*. [10], the onset of impervious disk reorientation can be modeled with exponential growth $\theta(t) = 5e^{\sigma N(t-t_c)/2\pi}$, where σ is the growth rate. Their experiments have shown that $\sigma = 2.7$ best matches the initial reorientation process. The dashed lines in Figs. 13(b) and 13(c) correspond to this model, where $\sigma = 2.7$ was taken according to the experiments. From Fig. 13(b), it can be seen that for the impervious case, this growth rate is in excellent agreement with our numerical results for early times. However, when increasing d/D_D, the growth rate decreases slightly for $d/D_D = 0.25$ and substantially when $d/D_D = 0.5$.

Figure 14 presents the time histories of the vorticity field ω_y for $\mathrm{Ar} = 49,\ \mathrm{Sc} = 7,\ \mathrm{Fr} = 11.4$ when (a) $d/D_D = 0$, (b) $d/D_D = 0.25$ and (c) $d/D_D = 0.5$. As the particle continues to decelerate after attaining its peak velocity, the vorticity magnitude in the caudal region associated with baroclinic torque decreases over time. Close to the disk centerline, a thin plume, which designates the region where $\omega_y = 0$ and separates the regions of positive and negative vorticity, can be seen for all three cases. Comparing Figs. 14(b) and 14(c) to 14(a), it can be seen that the transverse thickness of this plume increases with increasing d/D_D. More *et al.* [13] associated the reorientation observed in settling spheroids with the departure of the plume from the spheroid's centerline. A similar observation can be seen here at later times in Figs. 14(a) and 14(b), where as the disk begins to reorient, a shift in the position of the plume from close to the centerline of the disk toward the edge of the disk induces an additional torque on the disk, amplifying its reorientation [10]. Comparing the later time dynamics ($tU/R_{\mathrm{eq}} = 450$), it can be seen that when $d/D_D = 0$ and $d/D_D = 0.25$, the disks have at least started to reorient. However, this reorientation was not observed until later when $d/D_D = 0.5$ ($tU/R_{\mathrm{eq}} = 579$), as presented in Fig. 13(a).

The decrease in growth rate is directly related to the vorticity profile observed in Fig. 14. As the disk begins to reorient due to the dominance of the buoyancy torque over its hydrodynamic counterpart [13], the misalignment between the center of the plume and the center of the impervious disk accelerates the reorientation process. As d/D_D increases, the plume becomes transversely broader and the offset between the disk centerline and the plume center decreases, thus weakening the driving mechanism for accelerated reorientation.

Lastly, settling and rising bodies in density-stratified fluids experience enhanced drag due to stratification [5,6,10]. To estimate the enhanced drag in a density-stratified fluid, we adopt a quasisteady approximation during the broadside-on rising phase after the disks have attained their peak velocity. In Fig. 15(a), we plot the temporal evolution of the buoyancy force $F_B = \int_{V_p} \rho_f g \, \mathrm{d}V - \rho_p V_p g$, the total force in the rising direction $F_T = \rho_p V_p \ dV_z/dt$ and the hydrodynamic force in the rising direction $F_H = \int_S (\boldsymbol{\tau} \cdot \boldsymbol{n}) \cdot \boldsymbol{e}_z \, \mathrm{d}S$, where V_p and S are the particle volume and surface, $\boldsymbol{n}$ is the outward unit normal, $\boldsymbol{e}_z$ is the vertical unit vector, and $\boldsymbol{\tau}$ is the stress tensor excluding the background hydrostatic pressure. Figure 14(a) shows that the hydrodynamic and buoyancy forces dominate during the broadside-on rising phase, with F_T close to zero. The inset shows that $|a_z|R_{\mathrm{eq}}/U^2$ decreases rapidly after the initial transient and remains small over the interval used for the drag estimate. These observations support the quasisteady approximation. Neglecting added mass and history effects, an effective stratified drag coefficient (C_D^S) is defined following Yick *et al*. [5]:

$$C_D^S = \frac{2\left|\frac{\rho_p}{\rho_f(z)} - 1\right| gh}{V_z^2}. \tag{28}$$

Furthermore, an instantaneous Archimedes, Reynolds, and Froude numbers may be defined as

$$\mathrm{Ar}(z) = \sqrt{\frac{3}{16}} \frac{\sqrt{gh\left|\frac{\rho_p}{\rho_f(z)} - 1\right|\left(D_D^2 - d^2\right)}}{\nu}, \tag{29}$$

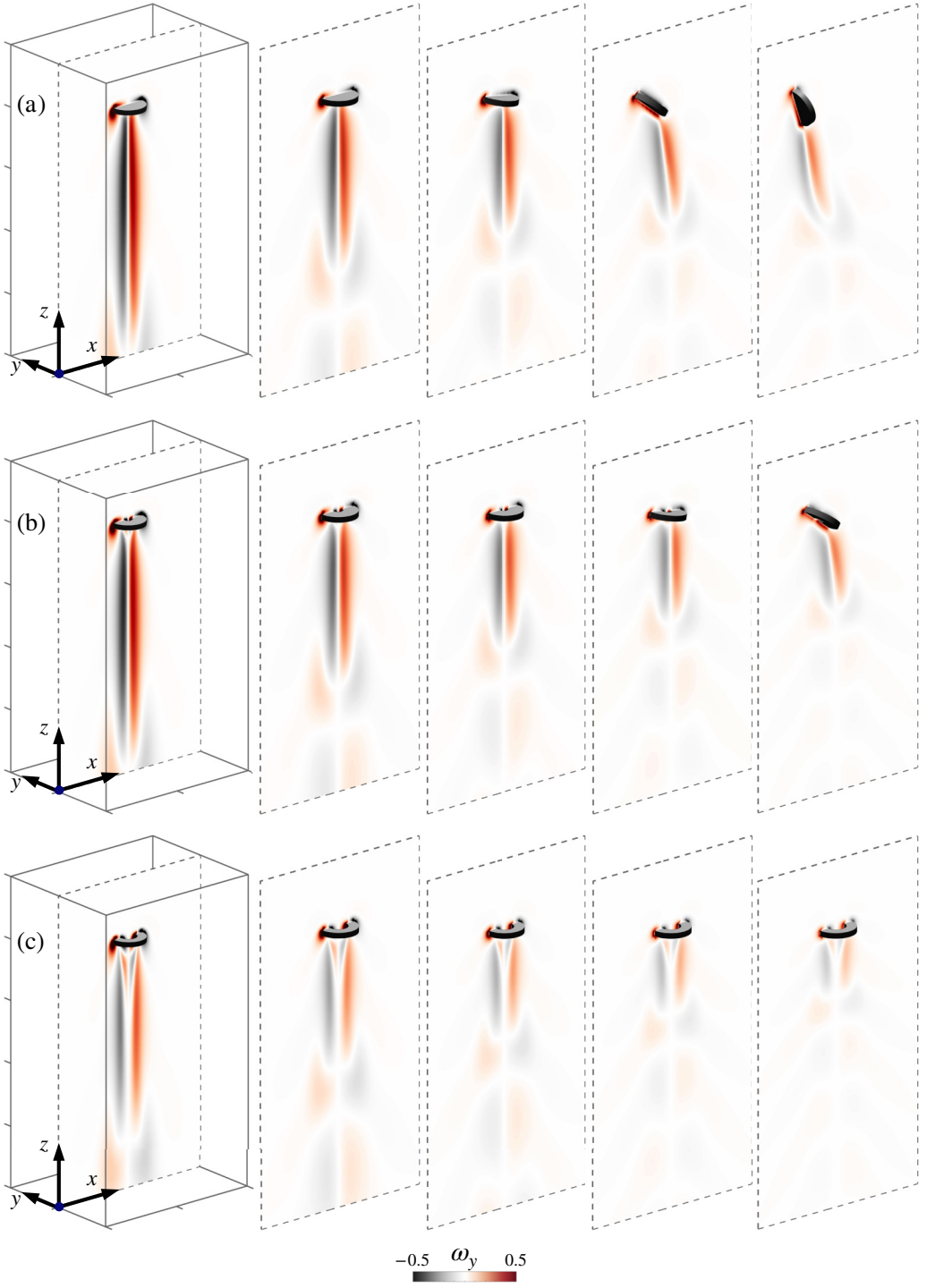


FIG. 14. Spatiotemporal evolution of the vorticity field ω_y for $\mathrm{Ar} = 49$, $\mathrm{Sc} = 7$, $\mathrm{Fr} = 11.4$ when (a) $d/D_D = 0$, (b) $d/D_D = 0.25$, and (c) $d/D_D = 0.5$. From left to right, $tU/R_{\mathrm{eq}} = [200,\ 300,\ 350,\ 400,\ 450]$.

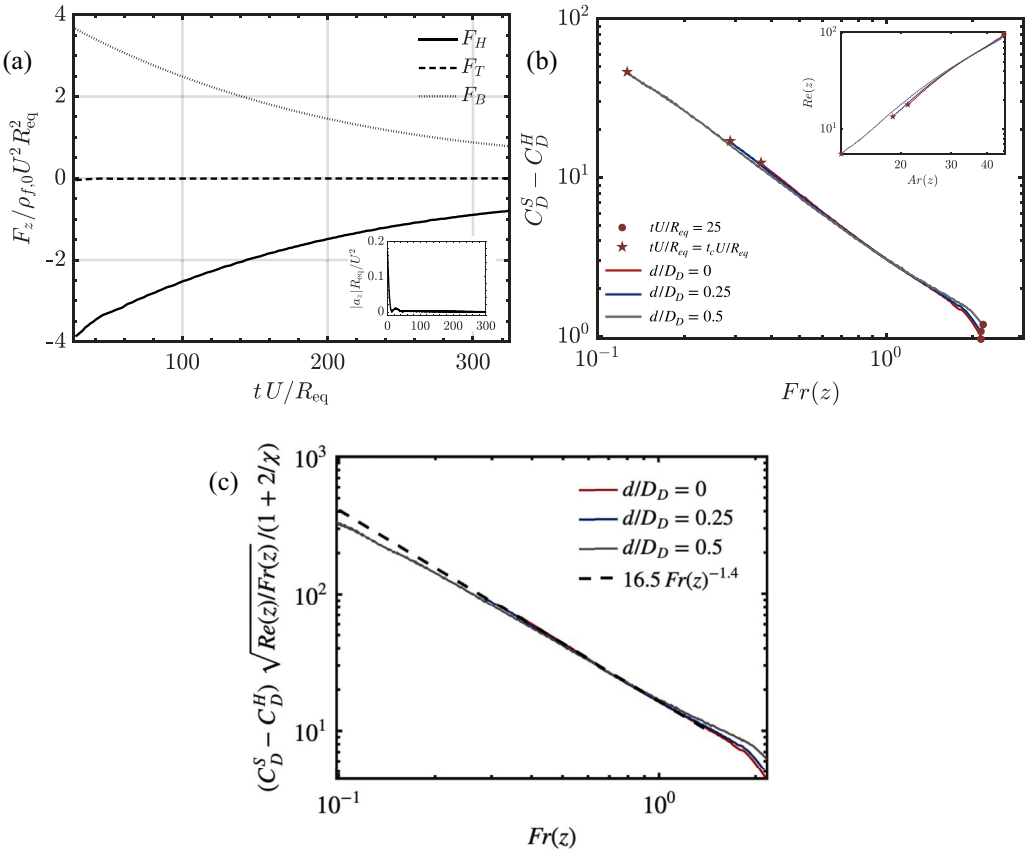


FIG. 15. (a) Force decomposition (z direction) from $tU/R_{\rm eq} = 25$ to $t = t_c$ when Ar $= 49$, Sc $= 7$, Fr $= 11.4$, and $d/D_D = 0$, illustrating quasisteady behavior. The inset in (a) shows the magnitude of the vertical acceleration, $|a_z|R_{\rm eq}/U^2$, where $a_z = dV_z/dt$, as a function of $tU/R_{\rm eq}$ for the same solid-disk case. (b) Evolution of $C_D^S - C_D^H$ as a function of the instantaneous Froude number Fr(z). The inset in (b) presents the instantaneous Reynolds against Archimedes numbers. Under the quasisteady state, $C_D^S = \frac{32}{3}\frac{\mathrm{Ar}(z)^2}{\mathrm{Re}(z)^2}$. The cases in (b) are for Ar $= 49$, Sc $= 7$, Fr $= 11.4$ and varying d/D_D. (c) Normalized stratification-induced drag enhancement, $(C_D^S - C_D^H)\sqrt{\mathrm{Re}(z)/\mathrm{Fr}(z)}/(1 + 2/\chi)$, as a function of the instantaneous Froude number Fr(z) for the same cases as in (b). The dashed line denotes the power-law fit $16.5\mathrm{Fr}(z)^{-1.4}$.

$$\mathrm{Re}(z) = \frac{|V_z|\sqrt{D_D^2 - d^2}}{\nu}, \tag{30}$$

$$\mathrm{Fr}(z) = \frac{|V_z|}{N\sqrt{D_D^2 - d^2}}. \tag{31}$$

A drag coefficient C_D^H defined previously in Eq. (21) can be utilized, as it models the drag coefficient of a disk in a homogeneous fluid (Fr $\to \infty$). Figure 15(b) presents $C_D^S - C_D^H$ when varying d/D_D as a function of Fr(z) from $tU/R_{\rm eq} = 25$ up to t_c. As $tU/R_{\rm eq} = 25$ corresponds to a time close to that at which the disks attain their maximum velocity, it corresponds to the point of highest Fr(z) and lowest $C_D^S - C_D^H$. As buoyancy effects become stronger, the stratification-induced drag coefficient increases as the particle speed decreases, which in turn reduces Fr(z). Figure 15(b) shows that the stratification

induced enhancement to the drag coefficient can be significantly larger than its homogeneous counterpart [10,13,31], with comparatively weak aperture dependence over the common range of instantaneous Froude numbers. A sensitivity check using 0%, 5%, and 10% endpoint adjustments gives median excess-drag differences from the solid disk of $1.3-1.5\%$ and $6.1-8.6\%$ at matched $\mathrm{Fr}(z)$, for $d/D_D = 0.25$ and 0.5, respectively. Changes in the wake structure accompanied by only modest drag changes were also reported by Cummins *et al.* [50] for permeable disks in a homogeneous fluid, where the recirculation zone behind the disk disappeared while the drag coefficient remained within 5% of the impervious disk value at $\mathrm{Re} = 130$. Increasing the aperture nevertheless delays reorientation, extending the broadside phase to smaller instantaneous Froude numbers and larger drag enhancement. The comparatively weak aperture dependence observed here is restricted to the investigated regime; different Reynolds, Froude, or Schmidt numbers, or larger apertures, may alter the balance of the mechanisms governing excess drag [6].

To compare the present stratification-induced drag with the scaling proposed by Mercier *et al.* [10], the same data are replotted in Fig. 15(c) using the normalized ordinate:

$$Y = \left(C_D^S - C_D^H\right)\frac{\sqrt{\mathrm{Re}(z)/\mathrm{Fr}(z)}}{1+2/\chi}. \tag{32}$$

This normalization is motivated by the model of Mercier *et al.* [10], in which the additional drag is associated with a thin shell of displaced fluid entrained with a solid disk. Their settling disks entrain lighter fluid; the rising disks considered here entrain heavier fluid. For a solid disk, the shell volume introduces the geometrical factor $(1+2/\chi)$, while the shell thickness scales as $\delta \sim \sqrt{\nu/N}$. With the diameter-based Reynolds and Froude numbers used in their analysis, this gives $\delta/D_D \sim \sqrt{\mathrm{Fr}/\mathrm{Re}}$. Rearranging their correlation gives

$$Y = a\mathrm{Fr}(z)^q, \tag{33}$$

with $a = 14 \pm 2$ and $q = -1.7 \pm 0.1$ over their fitted range $5 \leqslant \mathrm{Re} \leqslant 130$, $0.1 \leqslant \mathrm{Fr} \leqslant 3$, $70 \leqslant \mathrm{Sc} \leqslant 700$, and $3 \leqslant \chi \leqslant 10$. Here, the factor $(1+2/\chi)$ is retained as a solid-disk reference normalization for the annular cases. For the present annular disks, the instantaneous Reynolds and Froude numbers use the characteristic length $\sqrt{D_D^2 - d^2}$, so the comparison does not constitute a derivation of the entrained shell geometry for an annulus. The present solid and annular disk data approximately collapse under this normalization during the selected broadside rising phase. A power-law fit gives $Y = 16.5\mathrm{Fr}(z)^{-1.4}$, which is comparable in magnitude to the correlation of Mercier *et al.* [10] but has a shallower fitted exponent. The smaller Schmidt number considered here ($\mathrm{Sc} = 7$), together with differences in geometry and the sampled parameter range, may contribute to this difference; the present comparison does not isolate these effects. Moreover, $\mathrm{Re}(z)/\mathrm{Fr}(z) = N(D_D^2 - d^2)/\nu$ is constant along each trajectory, so this replot tests the combined variation along the trajectory rather than an independent Reynolds-number dependence.

IV. CONCLUDING REMARKS

This work investigates the rise dynamics of solid and annular disks in homogeneous and linearly stratified fluids at moderate Reynolds numbers. First, for impervious disks in a homogeneous fluid, our numerical results are benchmarked against the experiments of Fernandes *et al.* [19], showing excellent agreement for the homogeneous drag coefficient, C_D^H. For $\mathrm{Ar} = 49$ and $\mathrm{Ar} = 90$, introducing a central perforation leads to a transition from a fluttering trajectory to a rectilinear rise, consistent with the stabilizing influence of holes reported by Vincent *et al.* [23] at high Re. The stabilizing effect of perforation is quantified through the circulation Γ by isolating the contributions of the primary and secondary counterrotating vortex rings. In addition, perforation yields a slight increase in C_D^H, consistent with the reduced projected area.

In the linearly stratified cases, we analyze the wake dynamics by examining vorticity fields and centerline velocity profiles. Consistent with previous studies in stratified ambient fluids, the rise generates an additional detached toroidal vortex in the wake, attributable to the production

of baroclinic vorticity. Under sufficiently strong stratification (small Fr), disks and spheroids are known to undergo an orientational instability, transitioning from a broadside-on configuration to an edgewise orientation; this reorientation is also observed here. Increasing the size of the perforation, d/D_D, delays the onset of instability and reduces the critical velocity at which reorientation begins. The growth rate of this instability is found to decrease with increasing d/D_D, attributed to the alignment between the center of the disk and the stratification induced vortex plume.

The present results may be relevant to a range of oceanic settings in which stratification modifies both wake dynamics and body orientation. For example, the ability of stratification and perforations to suppress fluttering dynamics, while altering lateral dispersion, is directly relevant to the passive deployment of ocean-monitoring sensors and drifters for which platform orientation and trajectory stability are important [51].

Field measurements of marine snow provide a quantitative context for the present study. Drawing on the observations of MacIntyre *et al.* [3], Deepwell *et al.* [52] reported particle Reynolds numbers $\mathrm{Re} \simeq 0.2$–23 and Froude numbers $\mathrm{Fr} \simeq 5$–70 based on particle size and settling velocity. These ranges indicate that natural particles can experience appreciable inertia while interacting with stratified layers. The present simulations examine buoyant disks with an initial density ratio $\rho_p/\rho_{f,0} \simeq 0.99$, whose instantaneous Froude numbers decrease as they rise and decelerate. They therefore provide an idealized setting for examining how stratification modifies particle transport and orientation, processes relevant to the accumulation observed near density interfaces.

These findings also have implications for the transport of microplastics and other porous or damaged fragments in the ocean. A central aperture provides an idealized representation of a hole in a damaged particle rather than distributed porosity, and our results suggest that such geometric features can modify wake strength and delay the onset of reorientation near pycnoclines, potentially affecting residence times and lateral dispersion in stratified layers.

ACKNOWLEDGMENTS

This work was supported by the Engineering and Physical Sciences Research Council, UK, through the PREMIERE (Grant No. EP/T000414/1) program grant and the ANTENNA Prosperity Partnership grant (Grant No. EP/V056891/1). O.K.M. acknowledges funding from PETRONAS and the Royal Academy of Engineering for a Research Chair in Multiphase Fluid Dynamics. A.M.A. acknowledges the Kuwait Foundation for the Advancement of Sciences (KFAS) for their financial support. D.P. acknowledges support from the Imperial College London President Ph.D. scholarship. We acknowledge HPC facilities provided by the Imperial College London Research Computing Service. D.J. and J.C. acknowledge support through HPC/AI computing time at the Institut du Developpement et des Ressources en Informatique Scientifique (IDRIS) of the Centre National de la Recherche Scientifique (CNRS), coordinated by GENCI (Grand Equipement National de Calcul Intensif) Grant No. 2026 A0202B06721. The numerical simulations were performed with code BLUE [25].

DATA AVAILABILITY

There are no publicly available research data or software supporting this manuscript. Requests for further information or data should be sent to the authors.

[1] J. Magnaudet and M. J. Mercier, Particles, drops, and bubbles moving across sharp interfaces and stratified layers, Annu. Rev. Fluid Mech. **52**, 61 (2020).

[2] R. V. More and A. M. Ardekani, Motion in stratified fluids, Annu. Rev. Fluid Mech. **55**, 157 (2023).

[3] S. MacIntyre, A. L. Alldredge, and C. C. Gotschalk, Accumulation of marines now at density discontinuities in the water column, Limnology Oceanogr. **40**, 449 (1995).
[4] A. Doostmohammadi, S. Dabiri, and A. M. Ardekani, A numerical study of the dynamics of a particle settling at moderate Reynolds numbers in a linearly stratified fluid, J. Fluid Mech. **750**, 5 (2014).
[5] K. Y. Yick, C. R. Torres, T. Peacock, and R. Stocker, Enhanced drag of a sphere settling in a stratified fluid at small Reynolds numbers, J. Fluid Mech. **632**, 49 (2009).
[6] J. Zhang, M. J. Mercier, and J. Magnaudet, Core mechanisms of drag enhancement on bodies settling in a stratified fluid, J. Fluid Mech. **875**, 622 (2019).
[7] N. Abaid, D. Adalsteinsson, A. Agyapong, and R. M. McLaughlin, An internal splash: Levitation of falling spheres in stratified fluids, Phys. Fluids **16**, 1567 (2004).
[8] R. Camassa, L. Ding, R. M. McLaughlin, R. Overman, R. Parker, and A. Vaidya, Critical density triplets for the arrestment of a sphere falling in a sharply stratified fluid, in *Recent Advances in Mechanics and Fluid-Structure Interaction with Applications: The Bong Jae Chung Memorial Volume* (Springer, Berlin, 2022), pp. 69–91.
[9] S. Wang, P. Kandel, J. Deng, C.P. Caulfield, and S. B. Dalziel, Bouncing behaviour of a particle settling through a density transition layer, J. Fluid Mech. **997**, A49 (2024).
[10] M. J. Mercier, S. Wang, J. Péméja, P. Ern, and A. M. Ardekani, Settling disks in a linearly stratified fluid, J. Fluid Mech. **885**, A2 (2020).
[11] M. M. Mrokowska, Stratification-induced reorientation of disk settling through ambient density transition, Sci. Rep. **8**, 412 (2018).
[12] A. Doostmohammadi and A. M. Ardekani, Reorientation of elongated particles at density interfaces, Phys. Rev. E **90**, 033013 (2014).
[13] R. V. More, M. N. Ardekani, L. Brandt, and A. M. Ardekani, Orientation instability of settling spheroids in a linearly density-stratified fluid, J. Fluid Mech. **929**, A7 (2021).
[14] A. M. Abdal, L. Kahouadji, S. Shin, J. Chergui, D. Juric, C. P. Caulfield, and O. K. Matar, On the interaction between a rising bubble and a settling particle, J. Fluid Mech. **999**, A18 (2024).
[15] M. M. Mrokowska, Dynamics of thin disk settling in two-layered fluid with density transition, Acta Geophys. **68**, 1145 (2020).
[16] M. M. Mrokowska, Influence of pycnocline on settling behaviour of non-spherical particle and wake evolution, Sci. Rep. **10**, 20595 (2020).
[17] A. K. Varanasi, N. K. Marath, and G. Subramanian, The rotation of a sedimenting spheroidal particle in a linearly stratified fluid, J. Fluid Mech. **933**, A17 (2022).
[18] T. Lam, L. Vincent, and E. Kanso, Passive flight in density-stratified fluids, J. Fluid Mech. **860**, 200 (2019).
[19] P. C. Fernandes, F. Risso, P. Ern, and J. Magnaudet, Oscillatory motion and wake instability of freely rising axisymmetric bodies, J. Fluid Mech. **573**, 479 (2007).
[20] M. N. Ardekani, P. Costa, W. P. Breugem, and L. Brandt, Numerical study of the sedimentation of spheroidal particles, Int. J. Multiphase Flow **87**, 16 (2016).
[21] S. B. Field, M. Klaus, M. G. Moore, and F. Nori, Chaotic dynamics of falling disks, Nature (London) **388**, 252 (1997).
[22] F. Auguste, J. Magnaudet, and D. Fabre, Falling styles of disks, J. Fluid Mech. **719**, 388 (2013).
[23] L. Vincent, W. S. Shambaugh, and E. Kanso, Holes stabilize freely falling coins, J. Fluid Mech. **801**, 250 (2016).
[24] M. H. DiBenedetto, The fluid mechanics of ocean microplastics, Annu. Rev. Fluid Mech. **58**, 355 (2026).
[25] S. Shin, J. Chergui, and D. Juric, A solver for massively parallel direct numerical simulation of three-dimensional multiphase flows, J. Mech. Sci. Technol. **31**, 1739 (2017).
[26] L. Kahouadji, E. Nowak, N. Kovalchuk, J. Chergui, D. Juric, S. Shin, M. J. H. Simmons, R. V. Craster, and O. K. Matar, Simulation of immiscible liquid–liquid flows in complex microchannel geometries using a front-tracking scheme, Microfluid. Nanofluid. **22**, 126 (2018).
[27] E. A. Fadlun, R. Verzicco, P. Orlandi, and J. Mohd-Yusof, Combined immersed-boundary finite-difference methods for three-dimensional complex flow simulations, J. Comput. Phys. **161**, 35 (2000).

[28] H. Hanazaki, A numerical study of three-dimensional stratified flow past a sphere, J. Fluid Mech. **192**, 393 (1988).
[29] H. Hanazaki, K. Konishi, and T. Okamura, Schmidt-number effects on the flow past a sphere moving vertically in a stratified diffusive fluid, Phys. Fluids **21**, 026602 (2009).
[30] C. R Torres, H. Hanazaki, J. Ochoa, J. Castillo, and M. Van Woert, Flow past a sphere moving vertically in a stratified diffusive fluid, J. Fluid Mech. **417**, 211 (2000).
[31] A. M. Abdal, L. Kahouadji, S. Shin, J. Chergui, D. Juric, C.-C. P Caulfield, and O. K. Matar, Pairwise interaction of in-line spheroids settling in a linearly stratified fluid, Acta Mech. **236**, 5741 (2025).
[32] G. Corsi, P. G. Ledda, G. Vagnoli, F. Gallaire, and A. De Simone, Instability and trajectories of buoyancy-driven annular disks: A numerical study, Phys. Rev. Fluids **9**, 043907 (2024).
[33] P. Ern, F. Risso, D. Fabre, and J. Magnaudet, Wake-induced oscillatory paths of bodies freely rising or falling in fluids, Annu. Rev. Fluid Mech. **44**, 97 (2012).
[34] B. G. Inman, C. J. Davies, C. R. Torres, and P. J. S. Franks, Deformation of ambient chemical gradients by sinking spheres, J. Fluid Mech. **892**, A33 (2020).
[35] W. Zhang, D. Bi, and Y. Wei, Falling styles of perforated disks, Int. J. Multiphase Flow **161**, 104401 (2023).
[36] C. Lee, Z. Su, H. Zhong, S. Chen, M. Zhou, and J. Wu, Experimental investigation of freely falling thin disks. Part 2. Transition of three-dimensional motion from zigzag to spiral, J. Fluid Mech. **732**, 77 (2013).
[37] F. W. Roos and W. W. Willmarth, Some experimental results on sphere and disk drag, AIAA J. **9**, 285 (1971).
[38] C. Cummins, M. Seale, A. Macente, D. Certini, E. Mastropaolo, I. M. Viola, and N. Nakayama, A separated vortex ring underlies the flight of the dandelion, Nature (London) **562**, 414 (2018).
[39] J. B. Will, V. Mathai, S. G. Huisman, D. Lohse, C. Sun, and D. Krug, Kinematics and dynamics of freely rising spheroids at high Reynolds numbers, J. Fluid Mech. **912**, A16 (2021).
[40] R. Clift, J. R. Grace, and M. E. Weber, *Bubbles, particles and drops* (Academic Press, New York, 1978).
[41] A. J. Heymsfield and C. D. Westbrook, Advances in the estimation of ice particle fall speeds using laboratory and field measurements, J. Atmos. Sci. **67**, 2469 (2010).
[42] A. Tinklenberg, M. Guala, and F. Coletti, The settling of perforated disks in quiescent and turbulent air, J. Fluid Mech. **1010**, A34 (2025).
[43] J. Sánchez-Rodríguez and F. Gallaire, Tumbling elimination induced by permeability: An experimental approach, Phys. Rev. Fluids **10**, 013904 (2025).
[44] P. C. Fernandes, P. Ern, F. Risso, and J. Magnaudet, On the zigzag dynamics of freely moving axisymmetric bodies, Phys. Fluids **17**, 098107 (2005).
[45] W. Zhang, D. Bi, and Y. Wei, Effect of Archimedes number on the dynamics of free-falling perforated disks, Phys. Fluids **36**, 013324 (2024).
[46] H. K. Moffatt, Three coins in a fountain, J. Fluid Mech. **720**, 1 (2013).
[47] H. Zhong, C. Lee, Z. Su, S. Chen, M. Zhou, and J. Wu, Experimental investigation of freely falling thin disks. Part 1. The flow structures and Reynolds number effects on the zigzag motion, J. Fluid Mech. **716**, 228 (2013).
[48] M. Bayareh, A. Doostmohammadi, S. Dabiri, and A. M. Ardekani, On the rising motion of a drop in stratified fluids, Phys. Fluids **25**, 103302 (2013).
[49] K. B. Winters, P. N. Lombard, J. J. Riley, and E. A. D'Asaro, Available potential energy and mixing in density-stratified fluids, J. Fluid Mech. **289**, 115 (1995).
[50] C. Cummins, I. M. Viola, E. Mastropaolo, and N. Nakayama, The effect of permeability on the flow past permeable disks at low Reynolds numbers, Phys. Fluids **29**, 097103 (2017).
[51] P. Pounds, T. Potie, F. Kendoul, S. Singh, R. Jurdak, and J. Roberts, Automatic distribution of disposable self-deploying sensor modules, in *Experimental Robotics: The 14th International Symposium on Experimental Robotics* (Springer, 2015), pp. 535–543.
[52] D. Deepwell, R. Ouillon, E. Meiburg, and B. R. Sutherland, Settling of a particle pair through a sharp, miscible density interface, Phys. Rev. Fluids **6**, 044304 (2021).